energies

MDPI

Article

Thermoelectric Generation with Impinging Nano-Jets

Fatih Selimefendigil [1,*], Hakan F. Oztop [2] and Mikhail A. Sheremet [3,*]

[1] Department of Mechanical Engineering, Celal Bayar University, 45140 Manisa, Turkey
[2] Department of Mechanical Engineering, Technology Faculty, Fırat University, 23119 Elazığ, Turkey; hakanfoztop@firat.edu.tr
[3] Laboratory on Convective Heat and Mass Transfer, Tomsk State University, 634050 Tomsk, Russia
* Correspondence: fatih.selimefendigil@cbu.edu.tr (F.S.); sheremet@math.tsu.ru (M.A.S.)

Abstract: In this study, thermoelectric generation with impinging hot and cold nanofluid jets is considered with computational fluid dynamics by using the finite element method. Highly conductive CNT particles are used in the water jets. Impacts of the Reynolds number of nanojet stream combinations (between (Re_1, Re_2) = (250, 250) to (1000, 1000)), horizontal distance of the jet inlet from the thermoelectric device (between (r_1, r_2) = (−0.25, −0.25) to (1.5, 1.5)), impinging jet inlet to target surfaces (between w_2 and $4w_2$) and solid nanoparticle volume fraction (between 0 and 2%) on the interface temperature variations, thermoelectric output power generation and conversion efficiencies are numerically assessed. Higher powers and efficiencies are achieved when the jet stream Reynolds numbers and nanoparticle volume fractions are increased. Generated power and efficiency enhancements 81.5% and 23.8% when lowest and highest Reynolds number combinations are compared. However, the power enhancement with nanojets using highly conductive CNT particles is 14% at the highest solid volume fractions as compared to pure water jet. Impacts of horizontal location of jet inlets affect the power generation and conversion efficiency and 43% variation in the generated power is achieved. Lower values of distances between the jet inlets to the target surface resulted in higher power generation while an optimum value for the highest efficiency is obtained at location $z_h = 2.5w_s$. There is 18% enhancement in the conversion efficiency when distances at $z_h = w_s$ and $z_h = 2.5w_s$ are compared. Finally, polynomial type regression models are obtained for estimation of generated power and conversion efficiencies for water-jets and nanojets considering various values of jet Reynolds numbers. Accurate predictions are obtained with this modeling approach and it is helpful in assisting the high fidelity computational fluid dynamics simulations results.

Keywords: jet impingement; TEG; finite element method; nanofluid

check for updates

Citation: Selimefendigil, F.; Oztop, H.F.; Sheremet, M.A. Thermoelectric Generation with Impinging Nano-Jets. *Energies* **2021**, *14*, 492. https://doi.org/10.3390/en14020492

Received: 30 November 2020
Accepted: 14 January 2021
Published: 18 January 2021

Publisher's Note: MDPI stays neutral with regard to jurisdictional claims in published maps and institutional affiliations.

Copyright: © 2021 by the authors. Licensee MDPI, Basel, Switzerland. This article is an open access article distributed under the terms and conditions of the Creative Commons Attribution (CC BY) license (https://creativecommons.org/licenses/by/4.0/).

1. Introduction

Extensive research is dedicated to the studies related to progress of clean energy technologies and products during the recent years due to the cost of energy and environmental side effects. Therefore, many theoretical, practical and numerical simulation studies related to renewable energy technologies have been performed to develop energy efficient and small size products. Thermoelectric (TE) devices are integrated in many technological applications such as in waste heat recovery, military space, solar energy, refrigeration, thermal management and many others. They offer many advantageous such in compactness in size, low output noise, with no moving parts and they are also environmentally friendly. There are many parameters that affect their performances and effectiveness when used alone or integrated within a system for renewable energy applications such as the construction material, geometrical features of the module and legs, integrated thermofluid system fluid properties and its geometrical parameters. Pourkiaei et al. [1] presented the basic working principles with materials of thermoelectric generators and coolers. Advancements in the current technology and future challenges are also presented in this study. In another work, Karthick et al. [2] gave an overview for the application of thermoelectric generators (TEGs)

in solar energy and their effectiveness in the usage are also discussed in depth. TEG applications with photovoltaic systems in buildings are considered in the work of [3]. It is concluded that with the installation of TEG, significant energy savings can be obtained.

Jet impingement heat transfer is considered in many systems and locally higher heat and mass transfer coefficients are achieved with impinging jets [4–6]. There are many applications in practical thermal engineering systems including drying, textiles, some chemical processes, food industry, cooling of turbine blades, thermal treatment of surfaces and many others [7–12]. In jet impingement heat transfer, complex interaction takes place between the established vortices, boundary layer and pressure gradients. Depending on the geometry of thermo-fluid configuration, heat transfer fluid properties and boundary conditions, these interactions may even become more complicated. The effectiveness of the jet impingement heat transfer may be increased with the inclusion of nano-sized metallic or nonmetallic particles in the base fluid [13–15]. The technology of nanofluid is implemented in different thermal energy applications from solar power to electronic cooling [16–23]. Many advanced modeling techniques and complicated thermo-physical relations have been developed over the years for the accurate description of nanofluid behavior in thermal engineering systems [24–29]. There is a growing interest to use nanoparticles in jet impingement applications [30–36]. In a recent review work of Mohammadpour and Lee [37], recent advancements in the application of nanofluid jet impingement heat transfer are studied. Both numerical and experimental studies are covered while nanofluids application for conventional and swirling impinging jets are analyzed. Thermal transport features of base fluid with the inclusion of nano-sized particles will be enhanced and higher local and average heat transfer values are obtained in the jet impingement heat transfer configuration.

It is important to consider novel thermo-fluid configurations in order to achieve higher performances and power generations from the TEG integrated systems along with the latest developments in the construction materials of TEG modules and their geometrical parameters. In this work, we consider thermoelectric generation by a novel thermofluid configuration using impinging jets of hot and cold fluid streams. Highly conductive nano-sized CNT particles are also used in the base heat transfer fluid to increase the thermal conductivity and thermal transport. Confined slot jets with varying inlet velocities and solid volume fraction of nanoparticles are considered while a TEG module is located between the jets. The target surfaces of the TEG module are the hot and cold side of the interface surfaces. Owing to diverse use of jet impingement applications and widely use of TEGs in various engineering systems, the considered TEG integrated thermofluid system with nanoparticle inclusion is a novel contribution to the existing literature. The results of the present work will be helpful in the design and optimization of similar TEG integrated energy related products. In the present work, polynomial regression models are offered for the generated power and efficiency of the TEG device for various input parameters of interest and it is helpful to assist the 3D high fidelity CFD computations.

2. Numerical Model

Thermoelectric conversion for nanojet impingement is considered. Three dimensional and two dimensional configurations with boundary conditions are shown in Figure 1a,b. A thermoelectric generator (TEG) module is used that has target surfaces for the impinging nanojets of hot and cold fluid stream. The hot and cold fluid enters inlets with slot width of w_s while hot and cold uniform temperatures have values of T_h and T_c. The distance between the TEG interface surfaces and inlets is z_h. The horizontal location of the slot over the TEG device is also varying and the distances between the inlet slots to the device edges are $r_1 L_m$ and $r_2 L_m$ for hot and cold fluid streams with L_m denoting the length of the TEG module. The jets have uniform velocities of u_1 and u_2 at the inlets while distance between the outlets is L. The TEG device has legs with equal width, length and height of 2 mm. Conductor width, length and thickness are 4.5 mm, 2 mm and 0.2 mm, respectively

while the ceramic thickness is 0.3 mm. Table 1 presents the thermophysical properties of materials used in the TEG module.

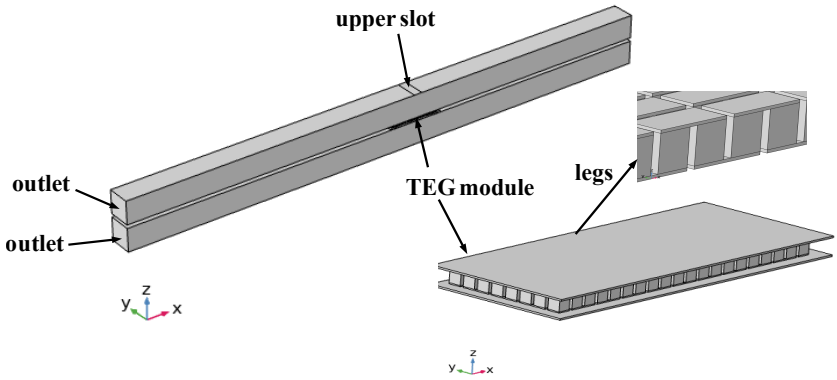

(**a**)

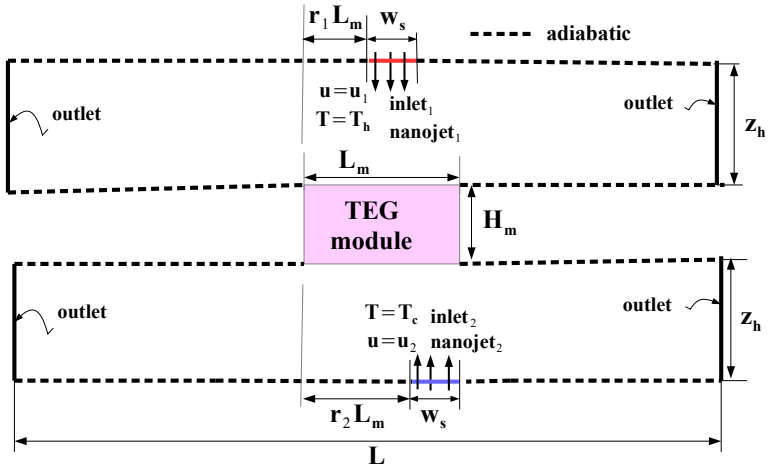

(**b**)

Figure 1. 3D schematic view of confined nanojet impinging system with TEG module (**a**) and 2D representation with boundary conditions (**b**).

Table 1. Material properties of thermoelectric generator (TEG) module.

	Symbol	P Type Leg (Bi_2Te_3)	N type leg (Bi_2Te_3)	Electrode (Copper)	Ceramic (Alumina)
Thermal conductivity	k (W/m K)	1.6	1.6	400	27
Electric conductivity	σ (S/m)	0.8×10^5	0.81×10^5	5.9×10^8	-
Seebeck coefficient	α (V/K)	2.1×10^{-4}	-2.1×10^{-4}	6.5×10^{-6}	-
Heat capacity	C_p (J/kg K)	154	154	385	900
Density	ρ (kg/m^3)	7700	7700	8960	3900

In the TEG device, conversion of the thermal energy into the electrical energy takes place. An important factor in the construction of the TEG devices is the figure of merit (ZT) and it is defined as:

$$ZT = \frac{\alpha^2 \sigma}{k} T. \quad (1)$$

Higher values of ZT are preferred when TEG integrated system is considered. TEG materials should have Seebeck coefficient (α), low thermal conductivity (k) and high

electrical conductivity (σ) values. Some of the available materials for the TEG devices are lead-telluride, bismuth-telluride and silicon germanium. For a couple, the open circuit voltage (V_{oc}) is defined as [38]:

$$V_{oc} = (\alpha_p - \alpha_n)\Delta T, \tag{2}$$

with α and ΔT denoting the Seebeck coefficient and temperature difference. The total TEG internal resistance is got from the summation of the pair resistances as [38]:

$$R_{int} = (R_p + R_n + 2R_c), \tag{3}$$

while the resistances of the pellets are obtained as:

$$R_{p,n} = \frac{L_{p,n}\rho_{p,n}}{A_{p,n}}. \tag{4}$$

In the above representation, $L_{p,n}$, $\rho_{p,n}$ and $A_{p,n}$ are the length, electrical resistivity and cross-sectional area of the pellets, respectively. The total resistance when a load resistance R_L is connected is given as:

$$R_t = R_{int} + R_L. \tag{5}$$

TEG output power is obtained by using the resistance and voltage as:

$$P = \left(\frac{(\alpha_p - \alpha_n)(T_h - T_c)}{R_t}\right)^2 R_L \tag{6}$$

When the values of internal resistance and load resistance are equal, the maximum power is obtained.

In the present work, coupled equations of fluid flow, heat transfer and electric field are solved simultaneously with the appropriate boundary conditions.

Energy conservation in the solid domain is written as [39]:

$$\nabla(k\nabla T) + \frac{J^2}{\sigma} - TJ \cdot \nabla\alpha = 0 \tag{7}$$

Electric charge continuity and TE effect with heat flow coupling are stated as:

$$\nabla \cdot J = 0, \tag{8}$$

$$E = \rho J + \alpha\nabla T, \tag{9}$$

$$q = \Pi J - k\nabla T. \tag{10}$$

where E, q, Π and J are the electric field, heat flux vector, Peltier coefficient and current density, respectively. Following relations are utilized:

$$\Pi = \alpha T, \tag{11}$$

$$J = \sigma(E - \alpha\nabla T) \tag{12}$$

The relation between E and V are stated as:

$$E = -\nabla V \tag{13}$$

In the confined jet flow region, parallel plates are used and the jets with hot and cold streams are directed to the TEG interface surface. In the construction of the nanojets, highly conductive CNT nano-sized particles are used in the water which is the base fluid. Incompressible and Newtonian fluid assumption are used even at the highest solid volume fraction of used nanoparticles. The flow is three dimensional, steady and laminar. At

Reynolds number of less than 1000, the flow shows laminar features [40]. Impacts of various effects such as thermal radiation, viscous dissipation and natural convection are ignored. Under the above described assumptions, governing equations for jet flow regions are stated as:

$$\frac{\partial u}{\partial x} + \frac{\partial v}{\partial y} + \frac{\partial w}{\partial z} = 0 \tag{14}$$

$$\frac{\partial u}{\partial t} + u\frac{\partial u}{\partial x} + v\frac{\partial u}{\partial y} + w\frac{\partial u}{\partial z} = -\frac{1}{\rho_{nf}}\frac{\partial p}{\partial x} + \nu_{nf}\left(\frac{\partial^2 u}{\partial x^2} + \frac{\partial^2 u}{\partial y^2} + \frac{\partial^2 u}{\partial z^2}\right) \tag{15}$$

$$\frac{\partial v}{\partial t} + u\frac{\partial v}{\partial x} + v\frac{\partial v}{\partial y} + w\frac{\partial v}{\partial z} = -\frac{1}{\rho_{nf}}\frac{\partial p}{\partial y} + \nu_{nf}\left(\frac{\partial^2 v}{\partial x^2} + \frac{\partial^2 v}{\partial y^2} + \frac{\partial^2 v}{\partial z^2}\right) \tag{16}$$

$$\frac{\partial w}{\partial t} + u\frac{\partial w}{\partial x} + v\frac{\partial w}{\partial y} + w\frac{\partial w}{\partial z} = -\frac{1}{\rho_{nf}}\frac{\partial p}{\partial z} + \nu_{nf}\left(\frac{\partial^2 w}{\partial x^2} + \frac{\partial^2 w}{\partial y^2} + \frac{\partial^2 w}{\partial z^2}\right) \tag{17}$$

$$\frac{\partial T}{\partial t} + u\frac{\partial T}{\partial x} + v\frac{\partial T}{\partial y} + w\frac{\partial T}{\partial z} = \alpha_{nf}\left(\frac{\partial^2 T}{\partial x^2} + \frac{\partial^2 T}{\partial y^2} + \frac{\partial^2 T}{\partial z^2}\right). \tag{18}$$

The hot and cold stream nanojets have different uniform velocities of u_1 and u_2 while the temperatures are T_h = 323 K and T_c = 303 K. No slip boundary conditions (BCs) are used for the walls of the plates as $u = v = w = 0$ while adiabatic wall BCs are assumed on those surfaces as $\frac{\partial T}{\partial n} = 0$. Electrical insulation BC ($n \cdot J = 0$) is utilized on all surfaces of solid model except the ceramics. Electrical potential is defined as zero ($V = 0$) at the ground and the current is zero at terminal.

The non-dimensional parameters of interest are the hot and cold fluid stream Reynolds number ($\mathrm{Re}_1 = \frac{2u_1 w_s}{\nu_f}$, $\mathrm{Re}_2 = \frac{2u_2 w_s}{\nu_f}$) and Prandtl number ($\mathrm{Pr} = \frac{\nu}{\alpha}$).

Highly conductive single walled-CNT particles with varying solid volume fractions are used in the water to obtain the hot and cold nanojet streams. Thermophysical properties of the base fluid and CNT-particles are given in Table 2. A single phase modeling approach for the nanofluid is adopted in the present work. The effective nanofluid thermophysical relations are given with the following correlations. Density (ρ) and specific heat (c_p) are described as [41]:

$$\rho_{nf} = (1-\phi)\rho_f + \phi\rho_p \tag{19}$$

$$(\rho c_p)_{nf} = (1-\phi)(\rho c_p)_f + \phi(\rho c_p)_p \tag{20}$$

The Brinkman viscosity is taken as the effective viscosity model of the nanofluid and it is given as [42]:

$$\mu_{nf} = \frac{\mu_f}{(1-\phi)^{2.5}} \tag{21}$$

This model is simple in form but it does not consider the impacts of particle size and temperature. However, many studies related to convective heat transfer used this model and it is also used here. However, for the effective thermal conductivity, an advanced model is preferred which takes into account the space distribution of carbon nanotubes. It is described as: [43]:

$$\frac{k_{nf}}{k_f} = \frac{(1-\phi) + 2\phi\frac{k_{CNT}}{k_{CNT}-k_f}\ln\frac{k_{CNT}+k_f}{2k_f}}{(1-\phi) + 2\phi\frac{k_f}{k_{CNT}-k_f}\ln\frac{k_{CNT}+k_f}{2k_f}} \tag{22}$$

Accurate results were obtained with the above given model when experimental data was used [43].

Table 2. Base fluid and nanoparticle properties.

Property	Water	Single-Walled CNT
ρ (kg/m^3)	997.1	2600
c_p (J/kg K)	4179	425
k (W/m K)	0.61	6600
μ (kg/ms)	8.55×10^{-4}	-

The solution of the governing equations with the appropriate boundary conditions are solved with a commercial finite element based solver COMSOL [44]. This code is very appropriate for the simulation of coupled multi-physics problems and many modules corresponding to different physics are available. In the current work, program modules such as conjugate heat transfer and AC/DC are used. The interface and coupling relations between different physics are automatically handled. The Galerkin weighted residual finite element procedure is utilized for the solution of the governing equations with boundary conditions as described above. The field variables of interest are approximated with Lagrange finite elements of various orders and the resulting residuals are set to be zero in an average sense. PARDISO direct solver is chosen while the convergence criteria is set to 10^{-6}.

The simulation of the coupled field equations requires intensive computational time in 3D configuration. Grid independence tests are performed to achieve the optimal grid that the minimum computational time with accurate results. The test results for the generated power of the TEG device are shown in Figure 2 with different grid sizes at Reynolds numbers of (Re_1, Re_2) = (250, 500) and (Re_1, Re_2) = (1000, 500). Grid system G4 with 1,214,223 number of tetrahedral element is selected for the subsequent computations. The mesh is refined near the walls and at the interfaces.

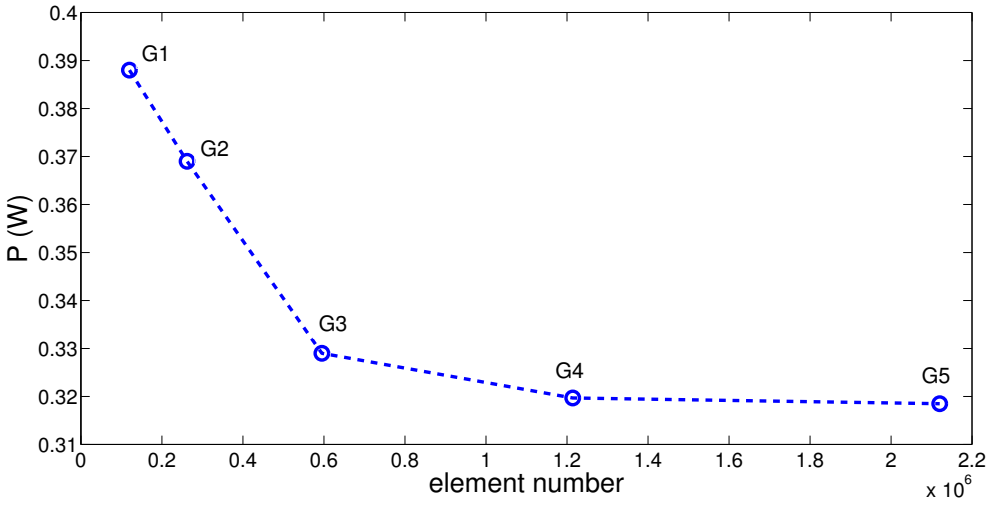

(**a**) (Re_1, Re_2) = (250, 500)

Figure 2. *Cont.*

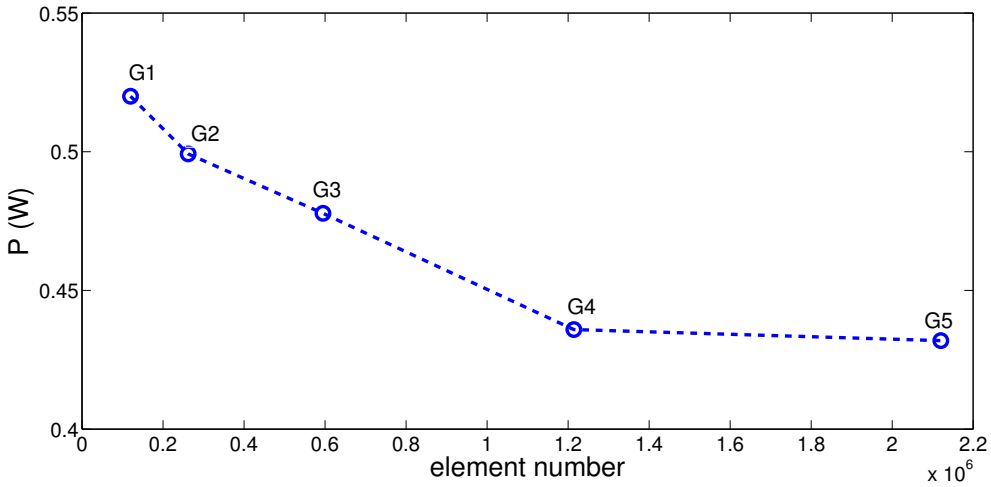

(**b**) (Re_1, Re_2) = (1000, 500)

Figure 2. Mesh independence test results for two different jet stream Reynolds number combinations ((r_1, r_2) = (1, 1), $z_h = 3w_s$, $\phi = 0.02$).

The numerical code is validated by using different sources available in the literature. In the first validation work, numerical results in Ref. [45] is used where jet impingement cooling in laminar flow regime is considered. Figure 3a shows the comparison results of the local Nusselt number variations at several locations along the target surface at Reynolds number of 100. In the second validation example, results related to jet impingement cooling of a surface with constant heat flux available in Ref. [46] are used. The average Nusselt number comparisons for two different aspect ratio are shown in Figure 3b. In these studies, the highest deviations are below 3% which shows the accuracy of the solver in jet impingement heat transfer problems. Another validation is included to show the capability of the code in simulating the thermoelectric effects and experimental values available in Ref. [47] are used. Comparison of the TEG power outputs for varying hot side temperatures while keeping the cold side is kept at 303 K is presented in Figure 4 and highest deviation of 8% is observed.

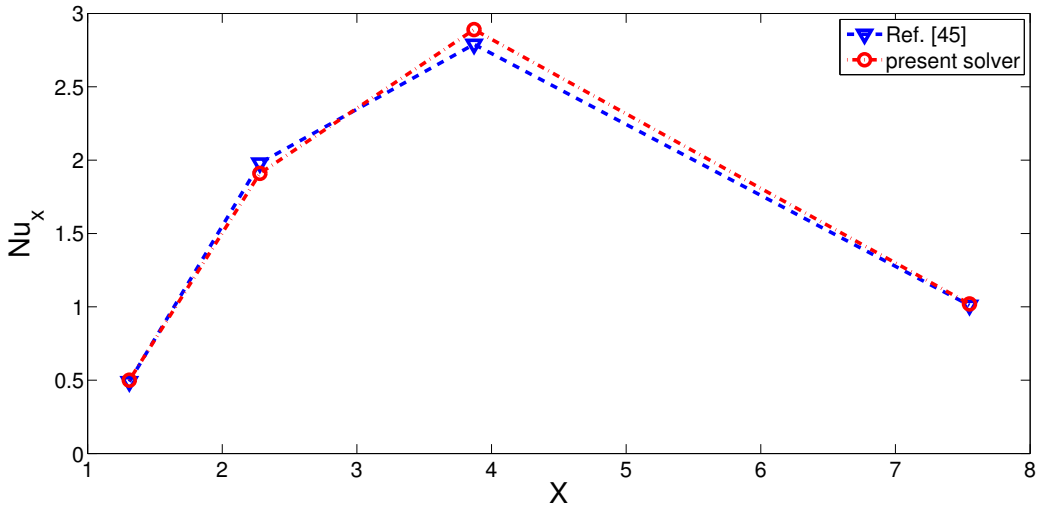

(**a**)

Figure 3. *Cont.*

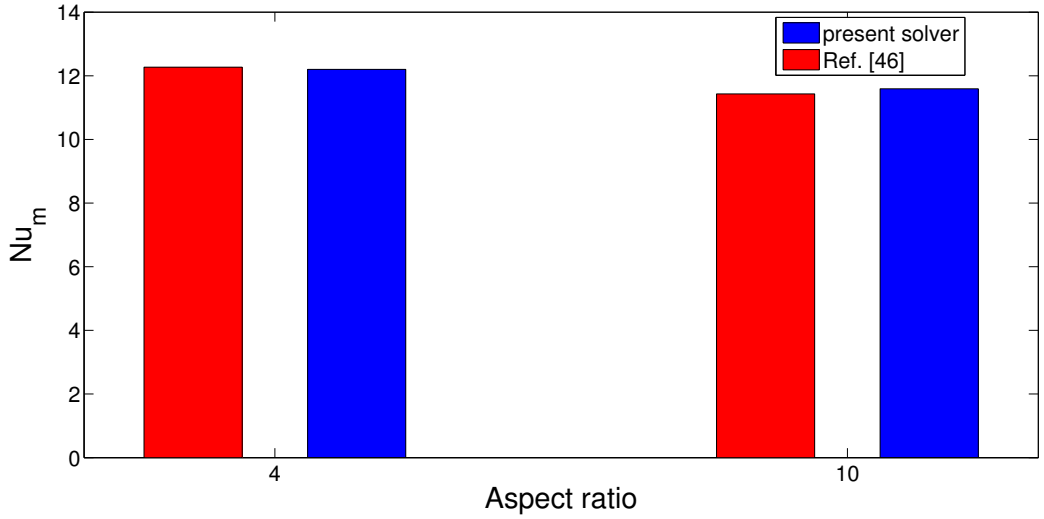

(**b**)

Figure 3. Comparison of local Nu number for various locations along the hot surface at Reynolds number of 100 with Ref. [45] (**a**) and average Nu number comparison for slot jet impingement cooling considering two values of aspect ratio at Reynolds number of 500 with Ref. [46] (**b**).

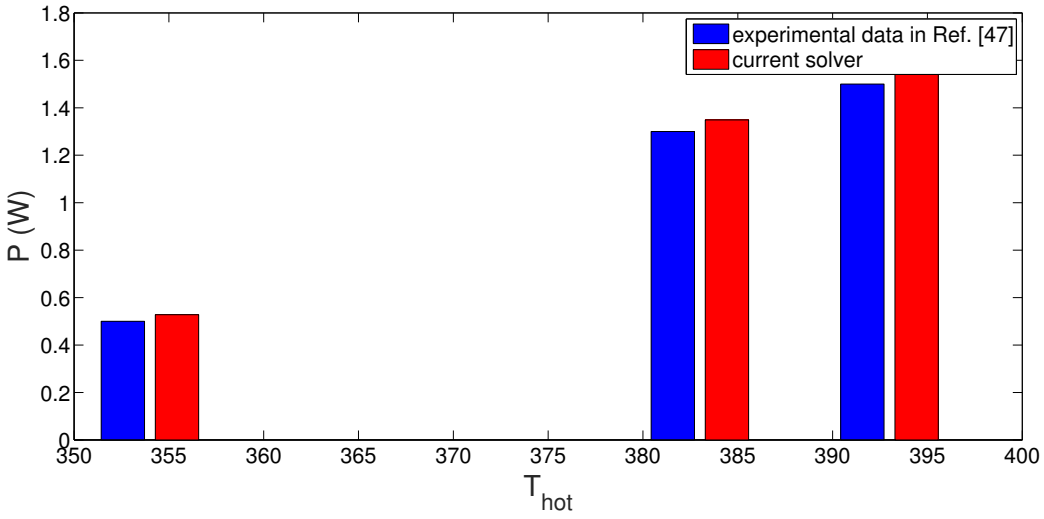

Figure 4. Comparison of generated TEG power with the present code and available results in Ref. [47].

3. Results and Discussion

Thermoelectric generation with nanojet impingement was considered. The target impinging surfaces were the hot and cold side of the TEG device. Nano-sized highly conductive CNT particles were used in confined slot jets that used water as the base fluid. Effects of Reynolds number of hot and cold nanojet stream combinations (between (Re_1, Re_2) = (250, 250) to (1000, 1000)), horizontal distance of the jets from the TEG surface (between (r_1, r_2) = (-0.25, -0.25) to (1.5, 1.5)), impinging jet inlet to target surfaces (between w_2 and $4w_2$) and solid nanoparticle volume fraction (between 0 and 2%) on the fluid flow, interface temperature variations, generated TEG power and efficiencies were numerically assessed. Polynomial based regression models were used for the estimation of generated power and efficiencies of the TEG device by using data from high fidelity computational fluid dynamics simulation results.

Figure 5 shows the effects of hot and cold nanojet stream Reynolds number combinations of (Re_1, Re_2) on the streamline distribution in the channels, electric potential and temperature variations within the TEG device ((r_1, r_2) = (1,1), $z_h = 3w_s$, $\phi = 0.02$). Recirculation regions were established near the inlets of the hot and cold jet streams due to the

entrainment and confinement effects. As the jet stream Reynolds number was increased, the size of the vortex increased while at the highest Reynolds number combinations secondary vortices away from the TEG device on the target surface were also established. The interface temperatures where hot and cold streams impinged varied with different Reynolds number combinations and this affected the electric potential and temperature distribution variation within the TEG device as shown in Figure 5g–l. There was 16% variation of the maximum electric potential when hot stream Reynolds number was increased from 250 to 1000. Peak values of hot and cold side temperatures also rose with higher fluid stream Reynolds numbers. Effects of hot jet stream Reynolds number on the variation of interface temperature of hot side and generated power are shown in Figure 6 with cold jet Reynolds number of 500. The hot side interface temperature and generated TEG output power rose with higher values of Re_1. The enhancement amount in the output power was 36% when cases with lowest and highest Re_1 were compared. As the higher values in the (Re_1, Re_2) Reynolds number combination were considered, hot side interface temperature increased while the cold side temperature decreased as shown in Figure 7. The net effect was the increment in the generated power of TEG device as shown in Figure 8a. When lowest and highest Reynolds number combinations for hot and cold jet streams were compared, there was an almost 81.5% increment in the generated output power. The efficiencies were also increasing with higher values of Re_1 and Re_2 while the values were in the range of 4.2% and 5.2% and the increment amount in the efficiency was approximately 23.8% (Figure 8b).

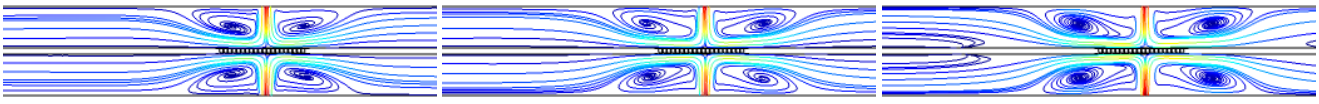

(**a**) Re_1 = 250, Re_2 = 250 (**b**) Re_1 = 500, Re_2 = 500 (**c**) Re_1 = 1000, Re_2 = 1000

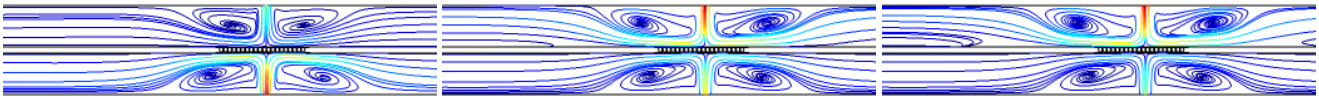

(**d**) Re_1 = 250, Re_2 = 500 (**e**) Re_1 = 500, Re_2 = 500 (**f**) Re_1 = 1000, Re_2 = 500

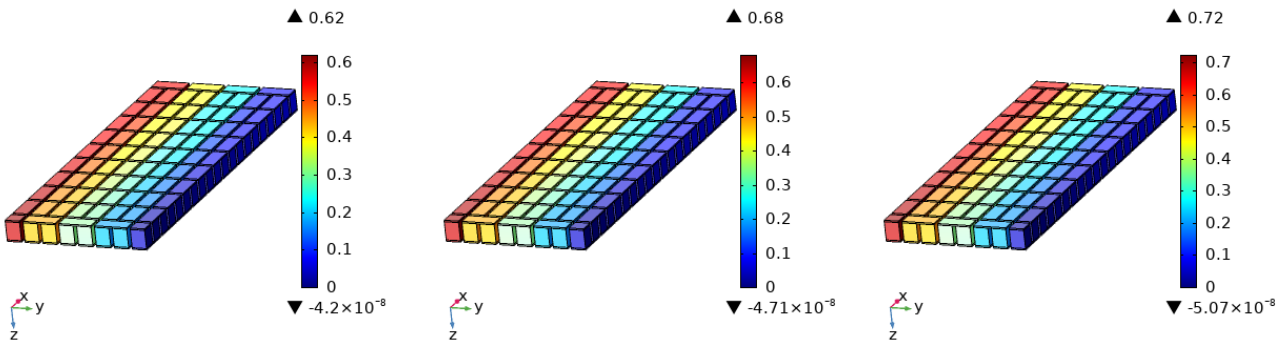

(**g**) Re_1 = 250, Re_2 = 500 (**h**) Re_1 = 500, Re_2 = 500 (**i**) Re_1 = 1000, Re_2 = 500

Figure 5. *Cont.*

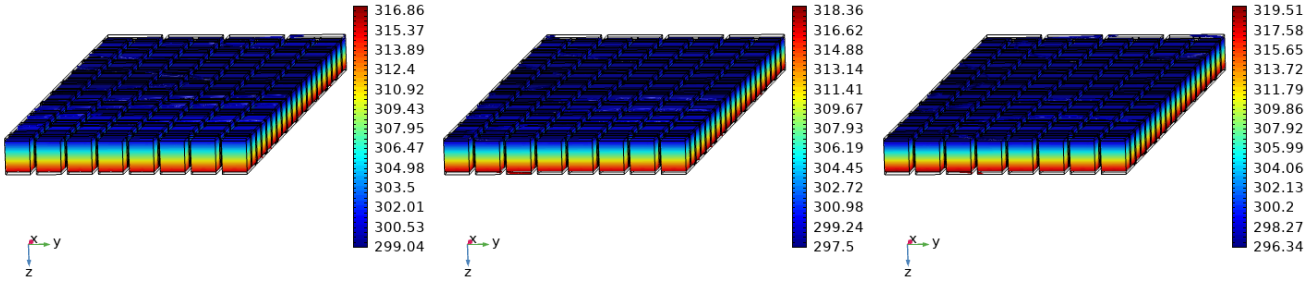

(**j**) Re_1 = 250, Re_2 = 500 (**k**) Re_1 = 500, Re_2 = 500 (**l**) Re_1 = 1000, Re_2 = 1000

Figure 5. Effects of different jet stream Reynolds number combinations on the variation of streamlines within the channels, electric potential and temperature distributions within the TEG module ((r_1,r_2) = (1,1), z_{lt} = 3w_s, ϕ = 0.02).

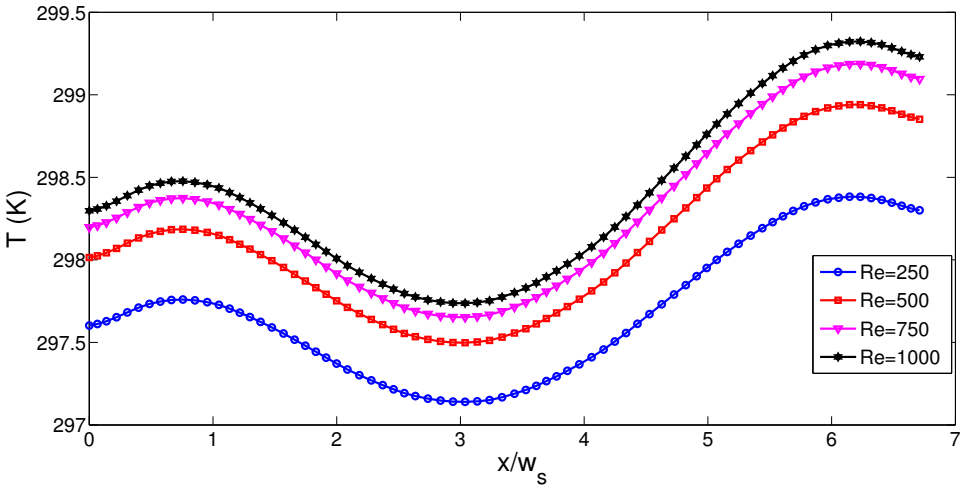

(**a**) cold side

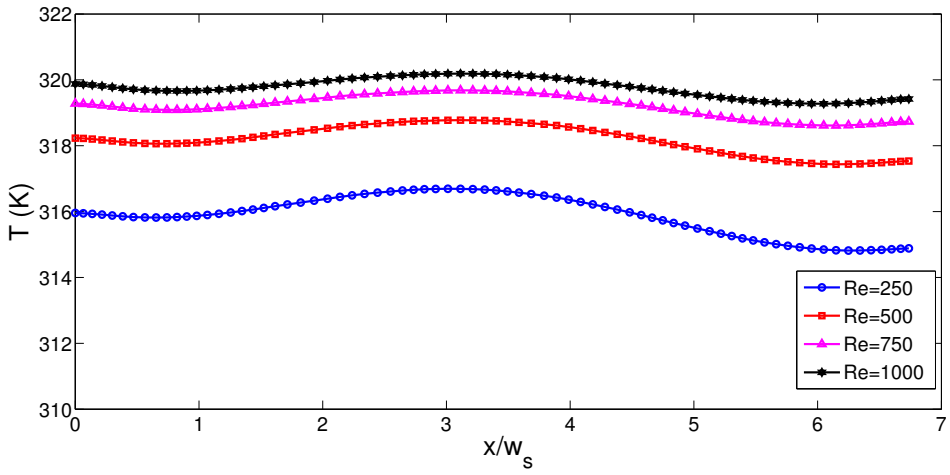

(**b**) hot side

Figure 6. *Cont.*

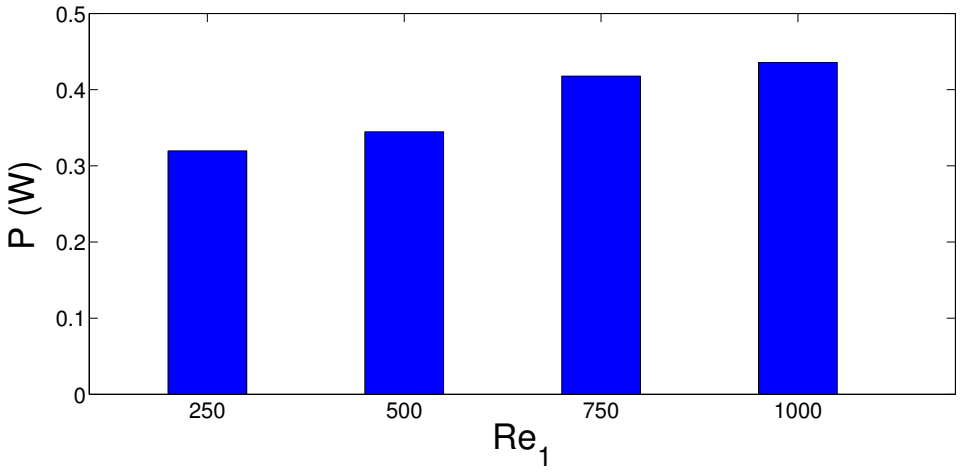

(**c**) power

Figure 6. Impacts of hot jet stream Reynolds number on the variation of interface temperatures of the cold and hot side (mid-axis) (**a**,**b**) and generated TEG power (**c**) (Re_2 = 500, (r_1,r_2) = (1,1), $z_h = 3w_s$, $\phi = 0.02$).

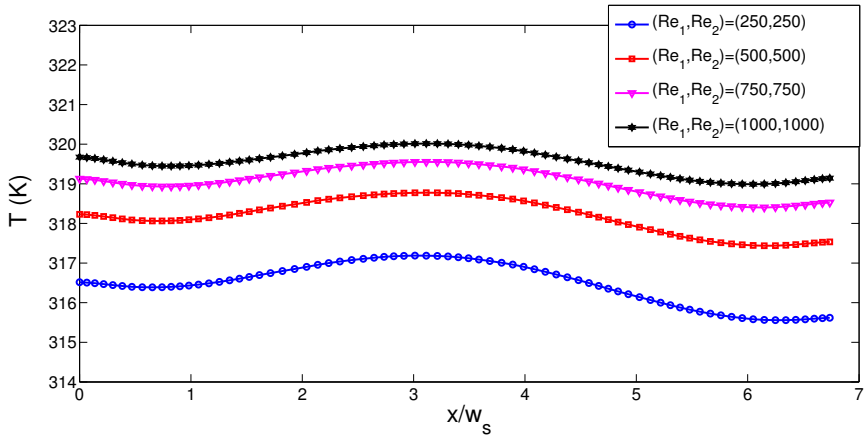

(**a**) hot

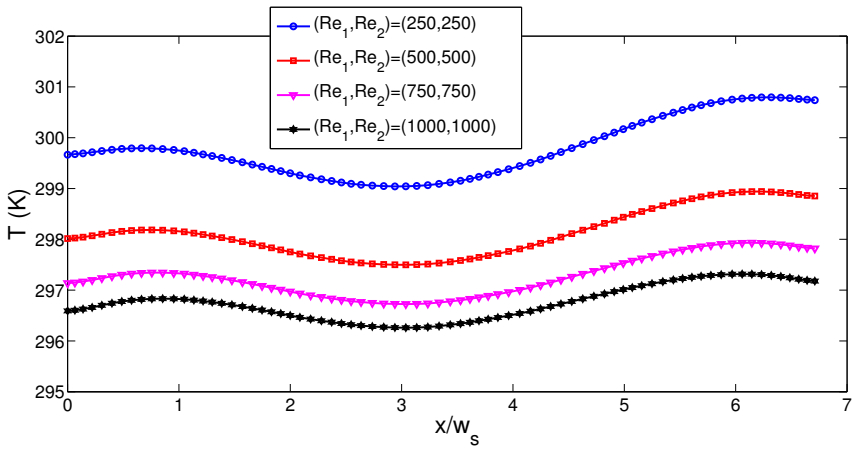

(**b**) cold

Figure 7. Effects of different jet stream Reynolds number combinations on the distribution of hot (**a**) and cold (**b**) interface temperatures (mid-axis) ((r_1, r_2) = (1, 1), $z_h = 3w_s$, $\phi = 0.02$).

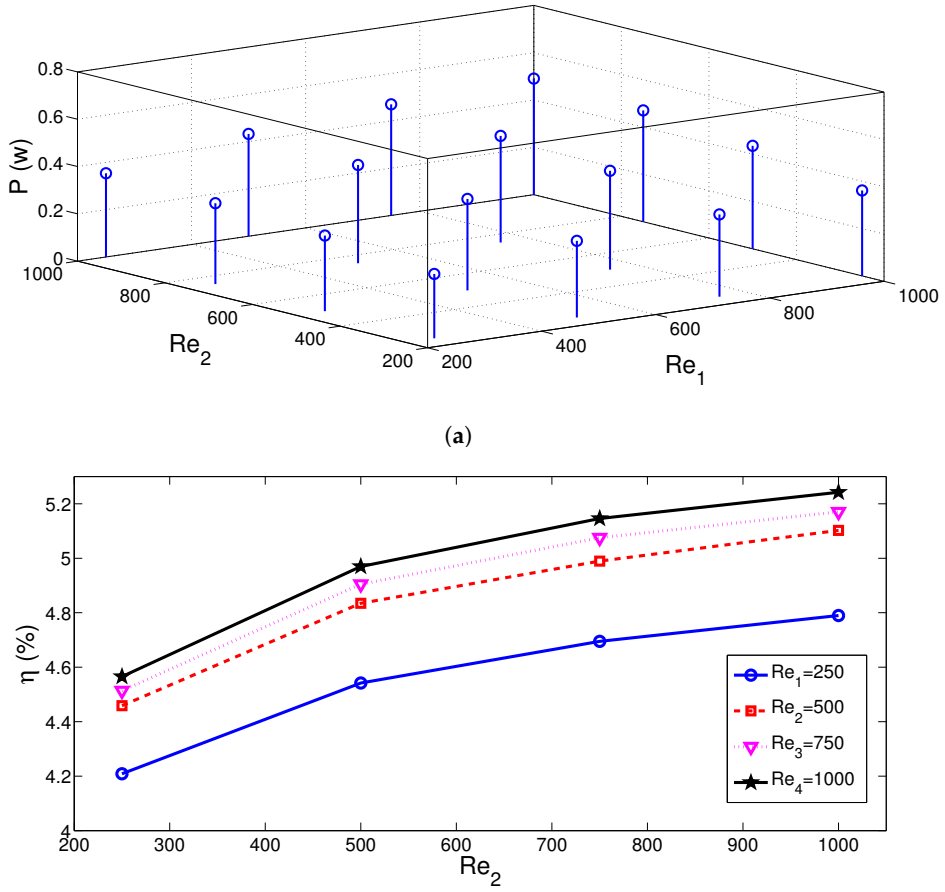

Figure 8. Generated powers (**a**) and efficiencies of the TEG device (**b**) with varying jet stream Reynolds number combinations ($(r_1, r_2) = (1, 1)$, $z_h = 3w_s$, $\phi = 0.02$).

The location of the jet stream inlet on the TEG device was important since the highest temperature at the interface between the TEG device and jet flow was obtained in this location. Therefore, horizontal location of the cold and hot jet streams were varied and their combined effects were included with the parameter combination of (r_1, r_2). As the the value of r_1 and r_2 were varied, the location of the impinging part and established vortex near the inlet jet are varied. Therefore, variation of interface temperature and electric potential/temperature field variation in the TEG device were influenced as shown in Figure 9d–f. Cold side interface temperature variations with varying horizontal locations of cold jet stream are presented in Figure 10. The location of the lowest temperatures and characteristics of local distribution of interface temperature were affected with varying r_1. Generated power characteristics and efficiency variations are given in Figure 11 with varying r_1 and r_2 values. When the hot jet stream location was fixed to $r_2 = 0.5$, the highest power was delivered for cold jet stream location at $r_2 = 1$. However, when different combinations of horizontal locations were considered, the lowest value of power was obtained at location $(-0.25, -0.25)$ while the highest one was attained at value of (1, 1). The variation in the generated TEG power at those locations was 43%. However, higher efficiencies were obtained with increasing the hot jet stream horizontal location from the TEG. When cases with $(r_1, r_2) = (0.5, -0.25)$ and $(r_1, r_2) = (0.5, 1.5)$ were compared, efficiency value rose from 2.8% to 11.40%.

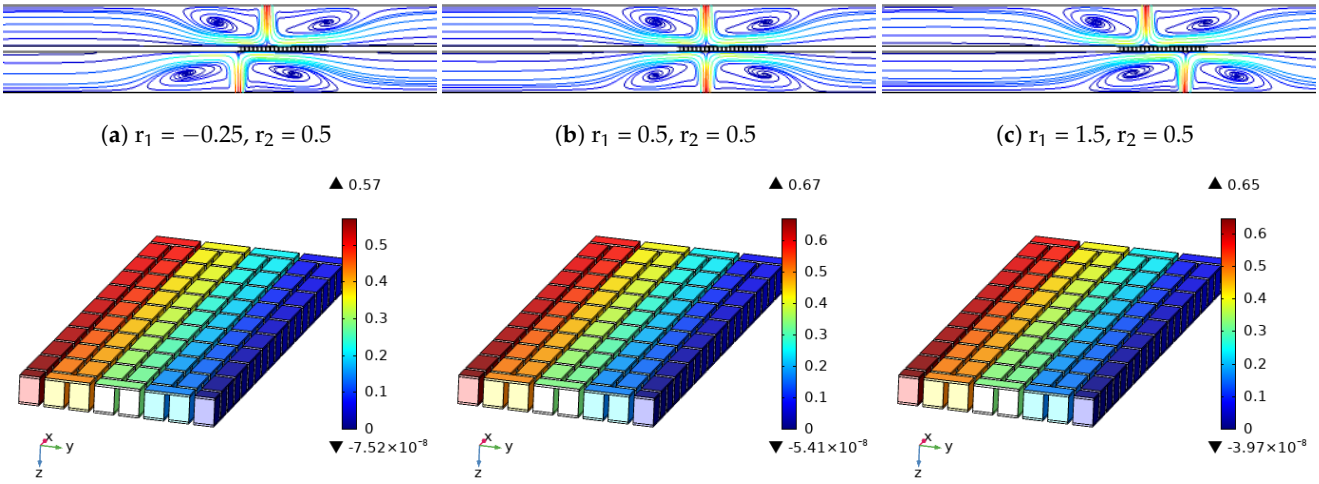

(**a**) $r_1 = -0.25$, $r_2 = 0.5$ (**b**) $r_1 = 0.5$, $r_2 = 0.5$ (**c**) $r_1 = 1.5$, $r_2 = 0.5$

(**d**) $r_1 = -0.25$, $r_2 = -0.25$ (**e**) $r_1 = 0.5$, $r_2 = -0.5$ (**f**) $r_1 = 1.5$, $r_2 = 1.5$

Figure 9. Effects of varying jet-stream inlet horizontal location combinations on the distribution of streamlines in the mid-plane channels (**a**–**c**) and electric potential variations in the TEG device (**d**–**f**) ((Re_1, Re_2) = (500, 500), $z_h = 3w_s$, $\phi = 0.02$).

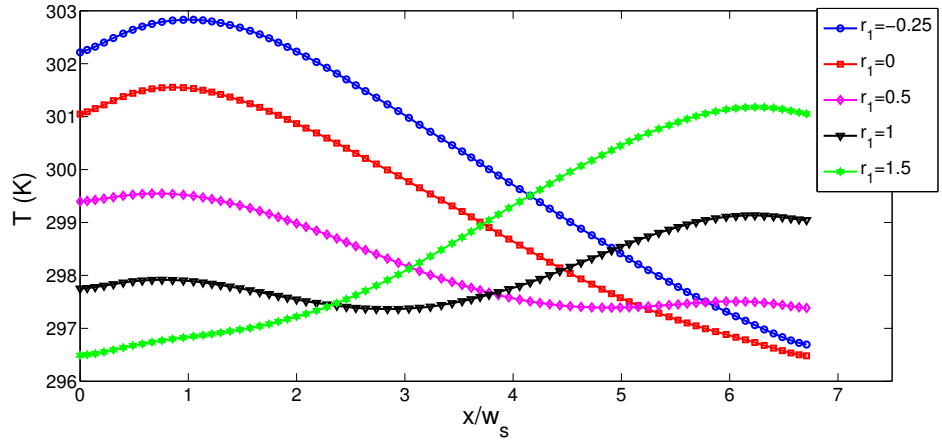

(**a**) cold side

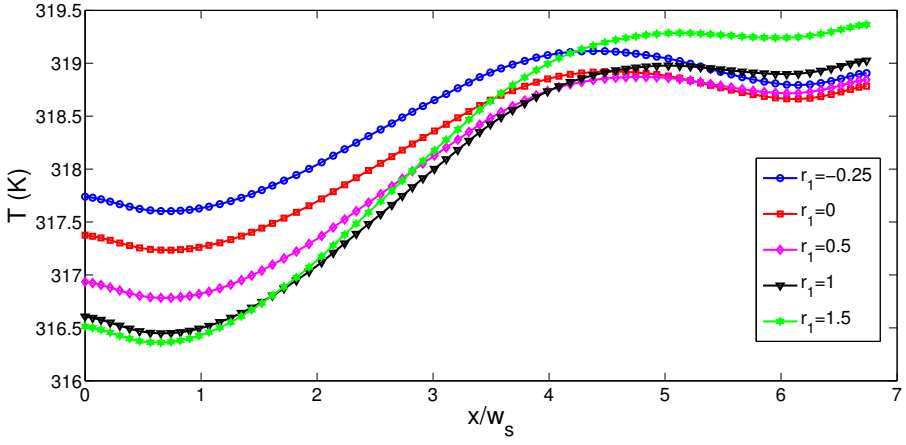

(**b**) hot side

Figure 10. Impacts of jet inlet horizontal location combinations on the variation of the interface temperatures at the cold (**a**) and hot side (**b**) of the TEG module ((Re_1, Re_2) = (500, 500), $z_h = 3w_s$, $\phi = 0.02$).

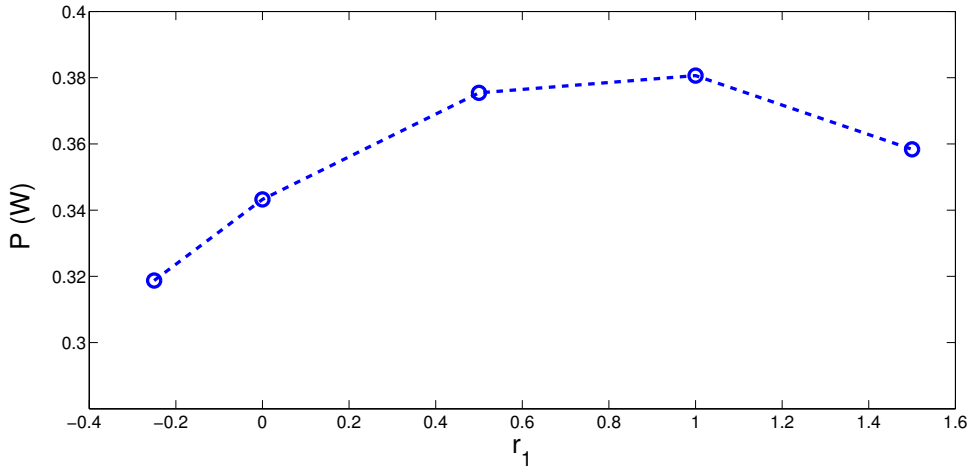

(**a**)

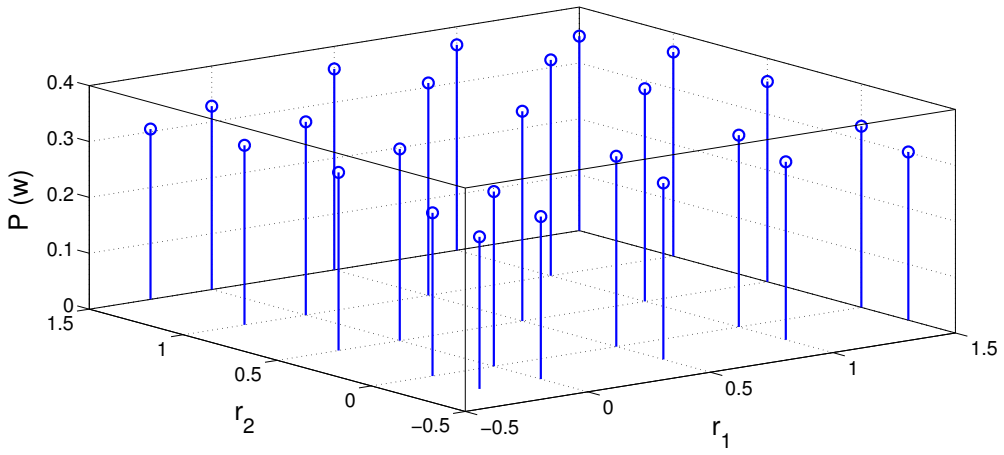

(**b**)

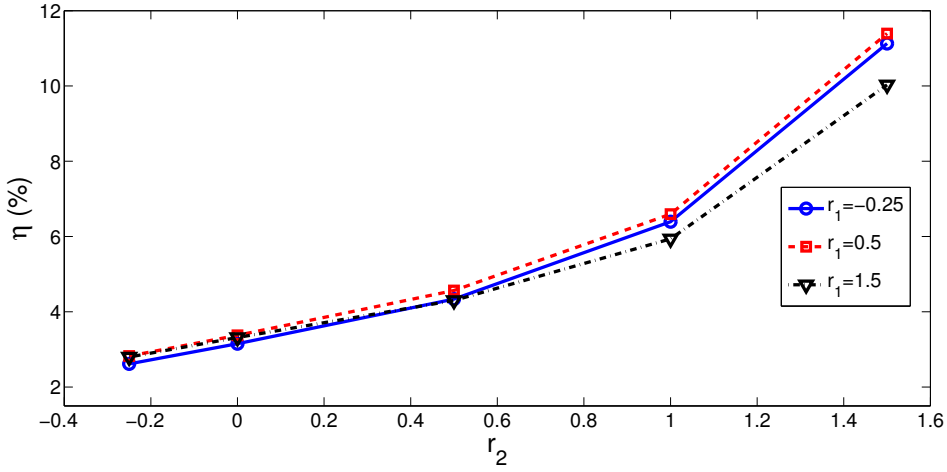

(**c**)

Figure 11. Generated powers (**a**,**b**) and efficiency (**c**) variation of the TEG device with respect to changes in the jet inlet horizontal location combinations ((Re_1, Re_2) = (500, 500), $z_h = 3w_s$, $\phi = 0.02$).

Another parameter of interest in the jet impingement thermoelectric generation is the distance from the jet stream inlet to target surface which is denoted by z_h. Cold side interface temperature dropped while hot side temperature rose with small values of distance of z_h (Figure 12) and therefore the net power generation in the TEG device increased as shown in Figure 13a. Here, 8% in the power enhancement was seen when cases with the smallest distance were compared with the highest one. However, the highest efficiency was obtained at distance of $z_h = 2.5w_s$ where 18% enhancement in the efficiency was achieved as compared to case with minimum efficiency at $z_h = w_s$.

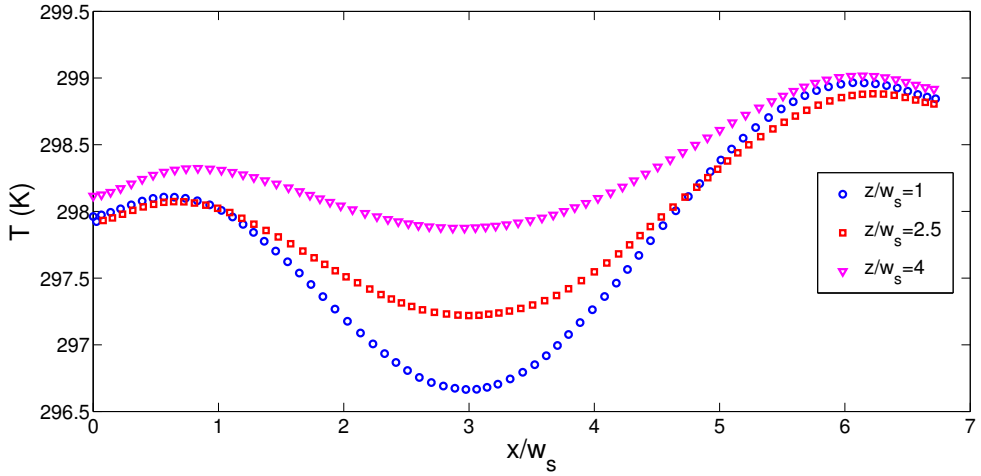

(**a**) cold side

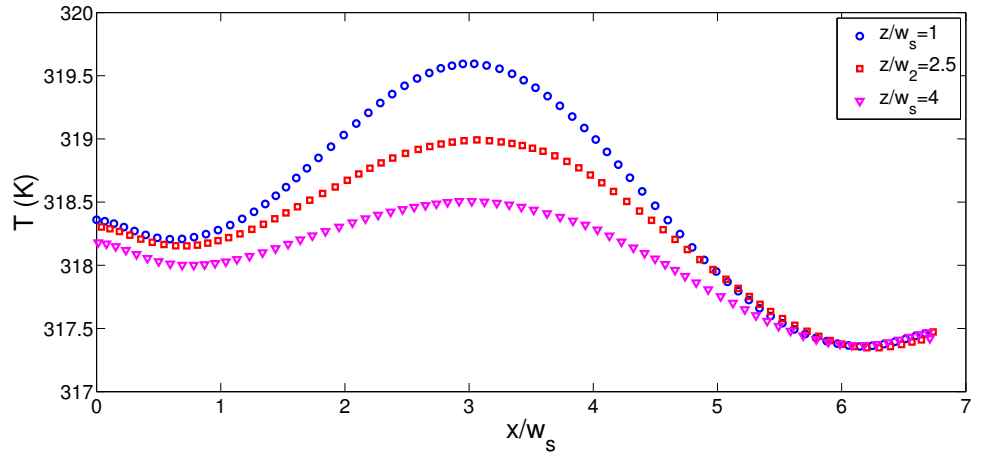

(**b**) hot side

Figure 12. Impacts of distance from the inlet to target surface on the variation of interface temperatures at the cold (**a**) and hot (**b**) side ((Re_1, Re_2) = (500, 500), (r_1, r_2) = (1, 1), $\phi = 0.02$).

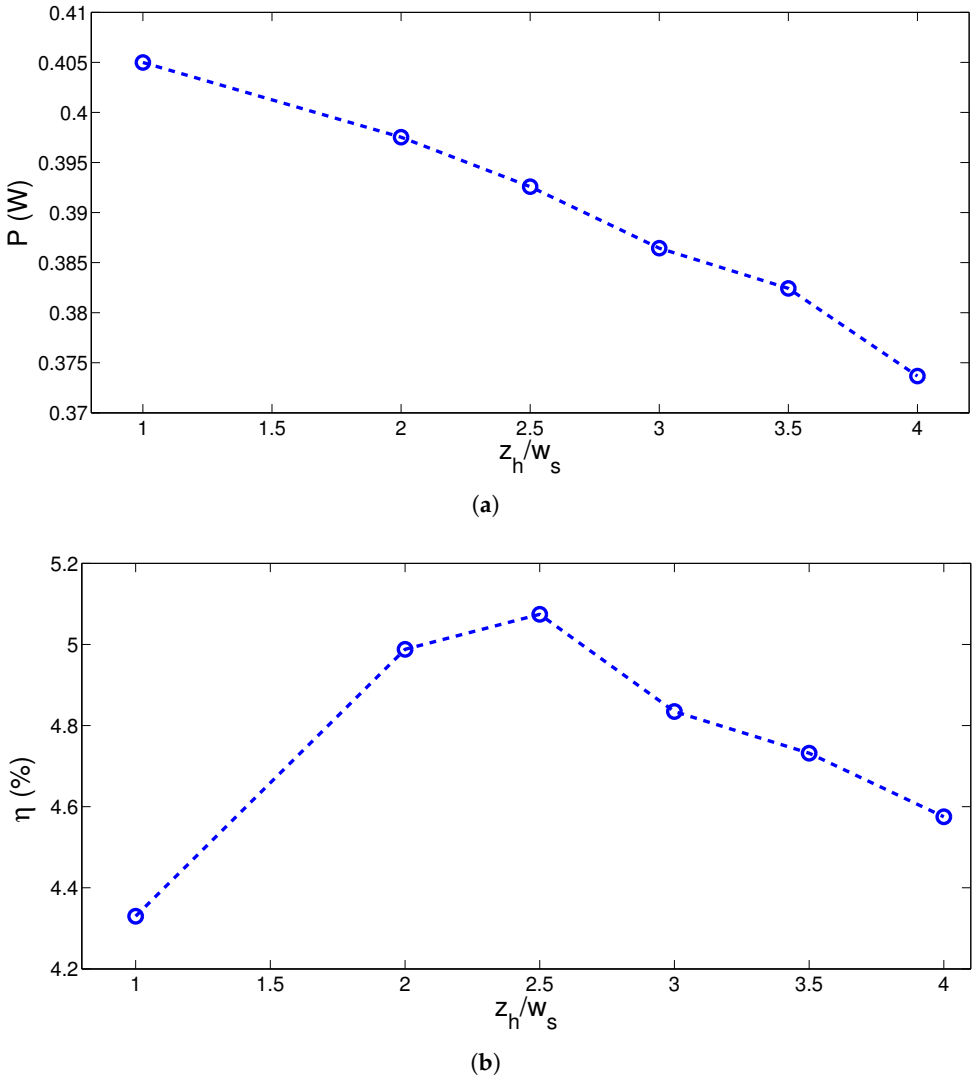

Figure 13. Generated power (**a**) and efficiency (**b**) of the TEG module with varying distance from the inlet to target surface ((Re_1, Re_2) = (500, 500), (r_1, r_2) = (1,1), $\phi = 0.02$).

Nanojet is formed by using highly conductive CNT particles in the water jet considering different solid volume fractions of particles. Thermal transport features are greatly enhanced which the inclusion of nanoparticles. Variation of hot and cold side interface temperatures with varying solid volume fraction of the particles are shown in Figure 14 ((Re_1, Re_2) = (500, 500), (r_1, r_2) = (1, 1), $z_h = 3w_s$). The cold side temperature dropped and hot side temperature rose throughout the TEG interface surface with higher ϕ. Generated power and efficiency versus varying solid volume fraction showed a linear increasing trend for different (r_1, r_2) combinations (Figure 15). As compared to using a pure water jet, power enhancements were in the range of 12% and 14% with nanojet at the highest particle volume fraction. Highest efficiency of 4.87% was achieved at r_1 = 1.5 with nanojet at the highest ϕ while the increment in the efficiency was only 3.5% as compared to the water jet.

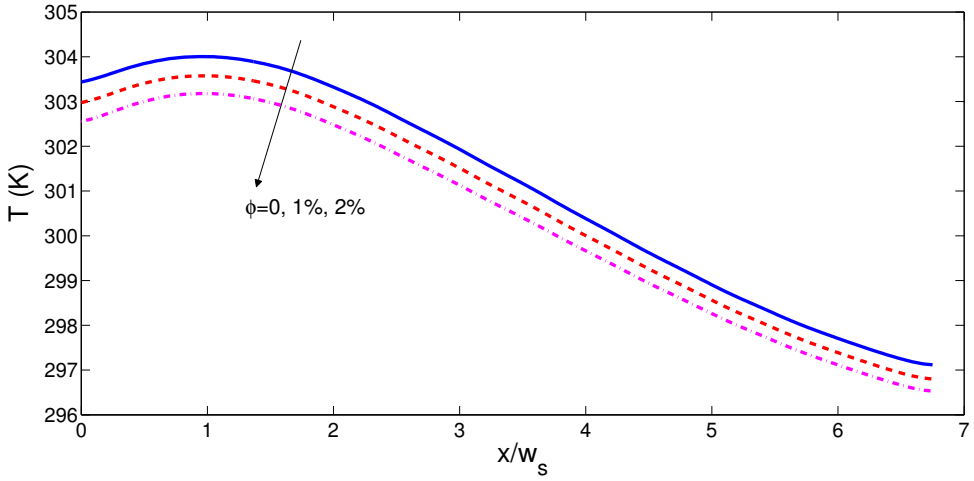

(**a**) cold side

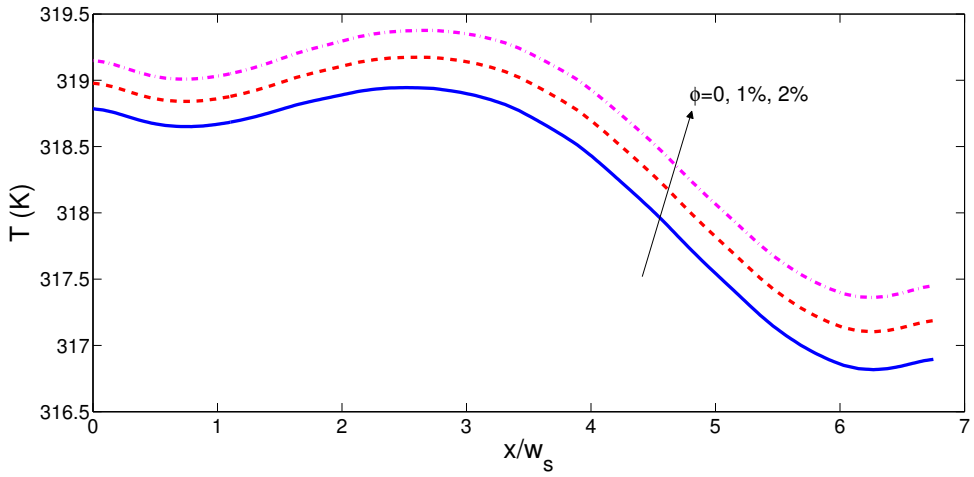

(**b**) hot side

Figure 14. Impacts of solid nanoparticle volume fractions of CNT on the variation of cold and hot interface temperatures ((Re_1, Re_2) = (500, 500), (r_1, r_2) = (1, 1), $z_h = 3w_s$).

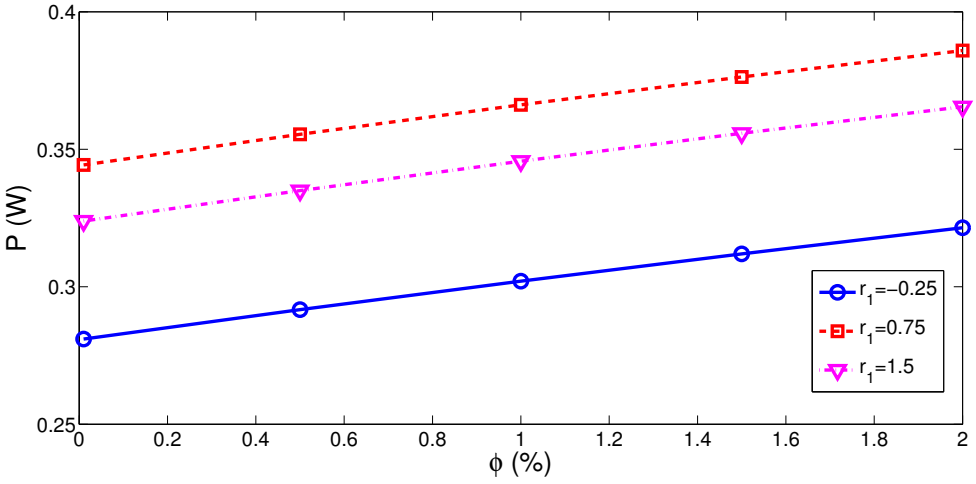

(**a**)

Figure 15. *Cont.*

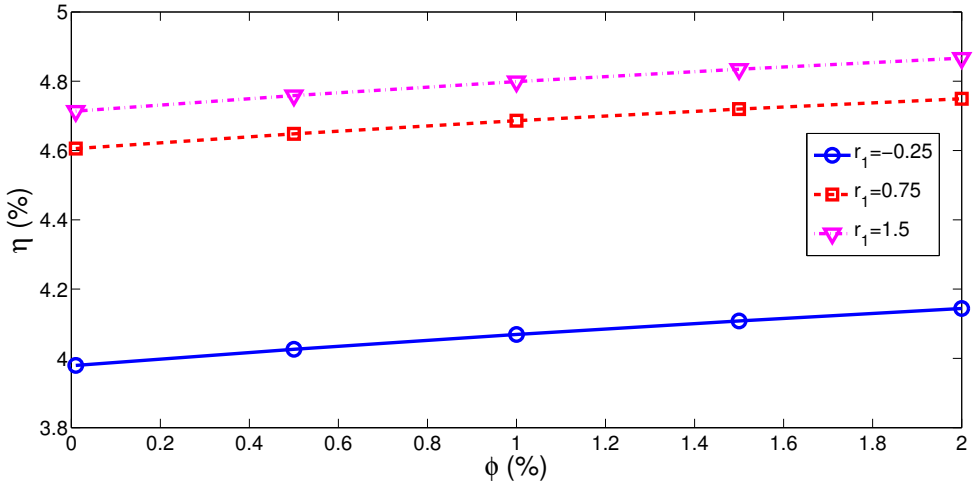

(**b**)

Figure 15. Generated power (**a**) and efficiency (**b**) of the TEG module with varying solid nanoparticle volume fractions of CNT and for different inlet horizontal distance of the hot jet stream ((Re_1, Re_2) = (500, 500), r_2 = 1, $z_h = 3w_s$).

Intensive computations were required for the solution of the coupled field equations of fluid flow, heat transfer and electric field in three dimensional configuration of jet impingement. It took about 9 hours in order to get the simulation results for one set of parametric combinations. For the estimation of generated TEG power and efficiency of the device, polynomial regression models were purposed. Two models were proposed for power estimation and two for efficiency predictions. As it is shown in the above given simulation results, power generation and efficiency versus nanoparticle showed almost linear relations. Therefore, regression models for pure water and nanofluid at the highest nanoparticle volume fractions were obtained. Linear interpolations among the polynomial coefficients could be used to determine coefficient of interest and estimated power or efficiency at any value of solid volume fraction within the maximum and minimum values. Data sets from numerical simulations corresponding to varying values of hot and cold jet stream Reynolds number between 250 and 1000 were collected. In total, 64 simulation results were used to construct the polynomial regression models. The polynomials were second order for each of the parameters (jet Reynolds numbers). The form of the output power and efficiency were given with polynomial coefficients as:

$$f(Re_{m1}, Re_{m2}) = p00 + p10 \times Re_{m1} + p01 \times Re_{m2} + p20 \times Re_{m1}^2 + p11 \times Re_{m1} \times Re_{m2} + p02 \times Re_{m2}^2 \quad (23)$$

with the modified hot and cold jet stream Reynolds number as $Re_m = \frac{\mathrm{Re}-625}{288.7}$. Tables 3 and 4 present the polynomial coefficients for the generated power and efficiency using water jet and nanojet. Goodness of the fit between the polynomial model output and CFD data could be described by R-square and RMSE (Root Mean Square Error). They were defined by using the following relations:

$$\mathrm{SSE} = \sum_{i=1}^{n} \left(y_i - y_i^p \right)^2 \quad (24)$$

$$\text{R-square} = 1 - \frac{\mathrm{SSE}}{\sum_{i=1}^{n} (y_i - \bar{y})^2} \quad (25)$$

$$\mathrm{RMSE} = \sqrt{\mathrm{SSE}/(n-m)} \quad (26)$$

where y_i, y_i^p, n and m denote the CFD output, polynomial output, number of response values and number of fitted coefficients, respectively. Table 5 shows the R-square values which are closer to 1 and lower values of RMSE. They indicated better fits for the predictions of generated power and efficiency.

Table 3. Coefficients (with 95% confidence bounds).

Coefficient	Value ($\phi = 0$)	Value ($\phi = 0.02$)
p00	0.3809 (0.3744, 0.3873)	0.4233 (0.4172, 0.4293)
p10	0.04377 (0.0405, 0.04704)	0.04445 (0.04136, 0.04754)
p01	0.04111 (0.03784, 0.04438)	0.04174 (0.03866, 0.04483)
p20	−0.01668 (−0.02091, −0.01246)	−0.01655 (−0.02054, −0.01256)
p11	0.007408 (0.00403, 0.01079)	0.006836 (0.003646, 0.01003)
p02	−0.0158 (−0.02002, −0.01157)	−0.01565 (−0.01963, −0.01166)

Table 4. Coefficients (with 95% confidence bounds).

Coefficient	Value ($\phi = 0$)	Value ($\phi = 0.02$)
p00	4.814 (4.767, 4.861)	4.981 (4.938, 5.025)
p10	0.09867 (0.07455, 0.1228)	0.1542 (0.1323, 0.1762)
p01	0.2611 (0.237, 0.2852)	0.2405 (0.2185, 0.2624)
p20	−0.05066 (−0.0818, −0.01951)	−0.07421 (−0.1025, −0.04591)
p11	0.01082 (−0.01409, 0.03574)	0.01314 (−0.009496, 0.03578)
p02	−0.09839 (−0.1295, −0.06724)	−0.0921 (−0.1204, −0.0638)

Table 5. Goodness of the fit for the polynomial models.

Fit Name	Value-Power ($\phi = 0$)	Value-Power ($\phi = 0.02$)
SSE	0.0003231	0.0002882
R-square	0.9946	0.9953
RMSE	0.005685	0.005368
Fit Name	**Value-Efficiency ($\phi = 0$)**	**Value-Efficiency ($\phi = 0.02$)**
SSE	0.01758	0.01452
R-square	0.9865	0.9894
RMSE	0.04193	0.0381

The surface/residual plots for the generated power and contour/residual plot for the efficiency with nanofluid are presented in Figures 16 and 17.

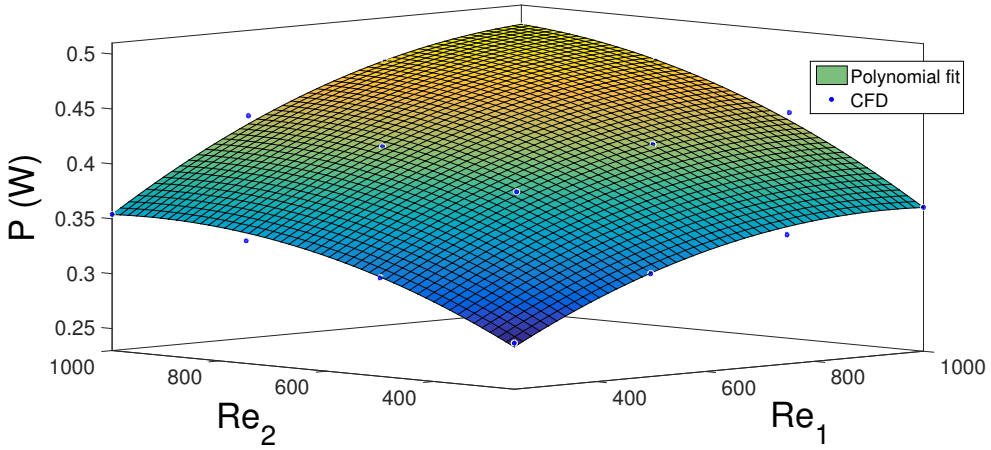

(**a**) surface plot

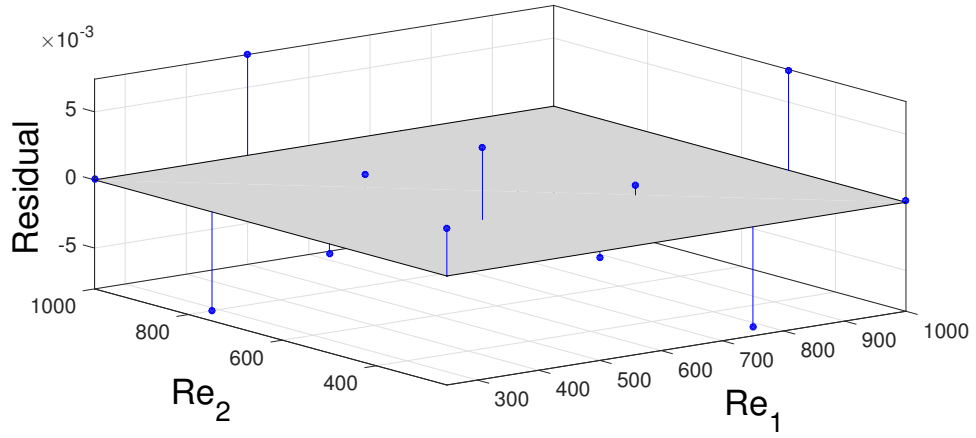

(**b**) residuals

Figure 16. Polynomial surface fit (**a**) and residual (**b**) plot for the generated TEG power with varying jet stream Reynolds numbers at $\phi = 0.02$.

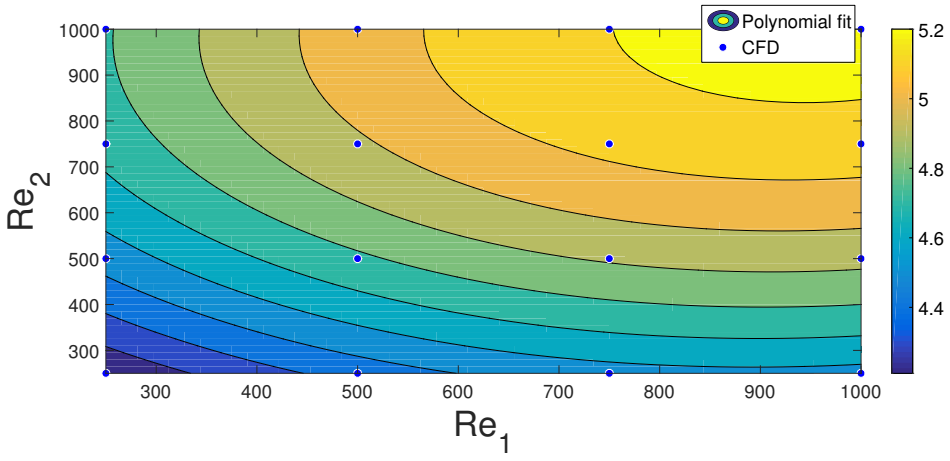

(**a**) contour

Figure 17. *Cont.*

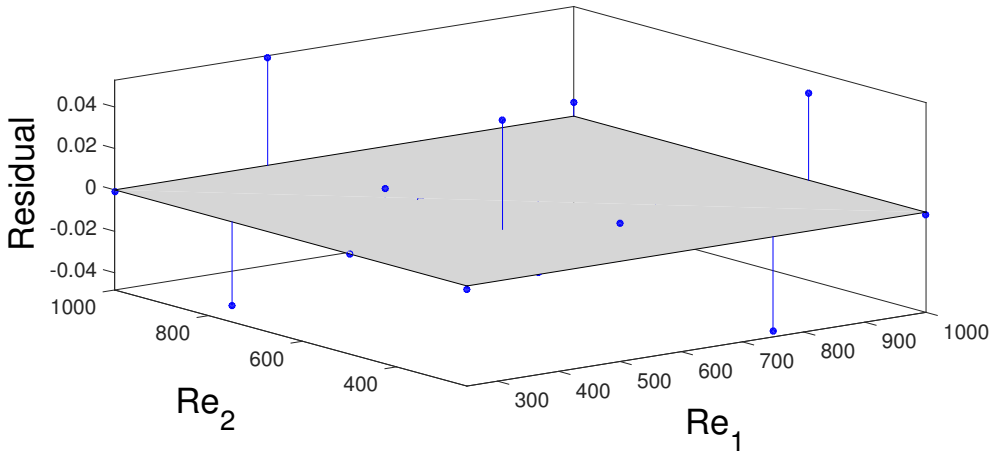

(**b**) residual

Figure 17. Contour plot (**a**) and residual (**b**) obtained with the polynomial fit for the efficiency of the TEG device with varying jet stream Reynolds numbers at $\phi = 0.02$.

4. Conclusions

Computational fluid dynamics simulation for thermoelectric generation with with impinging jets of hot and cold fluid streams is considered by using highly conducive CNT particles in the base fluid. The interface temperatures where hot and cold streams impinge change significantly with different Reynolds number combinations of hot and cold jet stream and this resulted in the electric potential and temperature distribution within the TEG device. Hot and cold jet streams Reynolds number variation resulted in higher power generation and conversion efficiencies. When lowest and highest Reynolds number combinations are compared, the generated power increases by 81.5% while the conversion efficiency rises by about 23.8%. Effects of horizontal location of the cold and hot jet streams on the TEG module are also varied during the simulation and their combined effects are considered. The lowest and highest power generation in the TEG module are achieved for hot and cold jet stream locations r_1 and r_2 of $(-0.25, -0.25)$ and (1, 1) while there is 43% variation in the generated power. However, the conversion efficiency changes from 2.8% to 11.40% with (r_1, r_2) from (0.5, −0.25) to (0.5, 1.5). When the distance from the inlet to the target impinge surface is increased, the generated power is decreased while the conversion efficiency behavior shows different characteristics with varying distance. There is 18% enhancement in the efficiency when lowest and highest efficiencies with distances at $z_h = w_s$ and $z_h = 2.5w_s$ are compared. Highly conductive nanoparticle inclusion resulted in enhancement in the generated power and conversion efficiency while the values of power rise is in the range of 12% and 14%. However, by using nano-jets with highest solid particle volume fractions, the efficiency rises only 3.5% as compared to water jet. The results indicated that the best performance in terms of generated power and efficiency are obtained at the highest value of Reynolds number pairs (Re_1, Re_2) = (1000, 1000) and at highest solid volume fraction of 0.02. However, the optimum values horizontal locations of the jets (r_1, r_2) and distance from the inlet to the target surface (z_h) are different in achieving the highest power and efficiency from the device. Polynomial type regression models for pure water and nanofluid at the highest nanoparticle volume fractions are achieved for the generated power and conversion efficiency. The models are valid for the whole range of hot and cold jet Reynolds numbers while linear interpolation between the polynomial coefficients can be used to cover the whole parametric variations in the nanoparticle volume fractions. These cheap models are helpful in obtaining fast and accurate results and assist the high fidelity computational fluid dynamics simulations which are computationally expensive.

Author Contributions: F.S. performed the numerical simulations and wrote some sections of the manuscript. H.F.O. and M.A.S. prepared some other sections of the paper and analyzed the results. All of the authors contributed equally for reviewing and revising the manuscript. All authors have read and agreed to the published version of the manuscript.

Funding: This research received no external funding.

Institutional Review Board Statement: Not applicable.

Informed Consent Statement: Not applicable.

Conflicts of Interest: The authors declare no conflict of interest.

Abbreviations

$A_{p,n}$	pellet cross-sectional area, (m^2)
a	length of corrugation, (m)
E	electric field intensity vector, (V/m)
H	channel height, (m)
h	local heat transfer coefficient, ($W/m^2 \cdot K$)
h	height of corrugation, (m)
J	electric current density vector, (A/m^2)
k	thermal conductivity, ($W/m^2 \cdot K$)
L	channel length, (m)
L_m	module length, (m)
N	number of corrugated waves
n	unit normal vector
Nu	Nusselt number
p	pressure, (Pa)
P	power output, (W)
Pr	Prandtl number
R_{int}	internal resistance, (Ω)
R_L	load resistance, (Ω)
Re	Reynolds number
T	temperature, (K)
u, v, w	x-y,z velocity components, (m/s)
V	voltage , (V)
W	channel width, (m)
x, y, z	Cartesian coordinates, (m)
ZT	figure of merit
Greek Characters	
α_{nf}	nanofluid thermal diffusivity, (m^2/s)
α	Seeback coefficient, (V/K)
μ	dynamic viscosity, (Pa·s)
ν	kinematic viscosity, (m^2/s)
ρ	density of the fluid, (kg/m^3)
σ	electrical conductivity, (S/m)
ϕ	solid volume fraction
η	efficiency
Subscripts	
c	cold wall
h	hot wall
m	average
nf	nanofluid

References

1. Pourkiaei, S.M.; Ahmadi, M.H.; Sadeghzadeh, M.; Moosavi, S.; Pourfayaz, F.; Chen, L.; Yazdi, M.A.P.; Kumar, R. Thermoelectric cooler and thermoelectric generator devices: A review of present and potential applications, modeling and materials. *Energy* **2019**, *186*, 115849. [CrossRef]
2. Karthick, K.; Suresh, S.; Hussain, M.M.M.; Ali, H.M.; Kumar, C.S. Evaluation of solar thermal system configurations for thermoelectric generator applications: A critical review. *Sol. Energy* **2019**, *188*, 111–142. [CrossRef]

3. Irshad, K.; Habib, K.; Saidur, R.; Kareem, M.; Saha, B.B. Study of thermoelectric and photovoltaic facade system for energy efficient building development: A review. *J. Clean. Prod.* **2019**, *209*, 1376–1395. [CrossRef]
4. Weigand, B.; Spring, S. Multiple jet impingement—A review. *Heat Transf. Res.* **2011**, *42*, 101–142. [CrossRef]
5. Krishan, G.; Aw, K.C.; Sharma, R.N. Synthetic jet impingement heat transfer enhancement—A review. *Appl. Therm. Eng.* **2019**, *149*, 1305–1323. [CrossRef]
6. Nadda, R.; Kumar, A.; Maithani, R. Efficiency improvement of solar photovoltaic/solar air collectors by using impingement jets: A review. *Renew. Sustain. Energy Rev.* **2018**, *93*, 331–353. [CrossRef]
7. Chen, Y.; Ma, C.; Qin, M.; Li, Y. Theoretical study on impingement heat transfer with single-phase free-surface slot jets. *Int. J. Heat Mass Transf.* **2005**, *48*, 3381–3386. [CrossRef]
8. Tepe, A.Ü.; Yetişken, Y.; Uysal, Ü.; Arslan, K. Experimental and numerical investigation of jet impingement cooling using extended jet holes. *Int. J. Heat Mass Transf.* **2020**, *158*, 119945. [CrossRef]
9. Aldabbagh, L.B.Y.; Mohamad, A.A. A three-dimensional numerical simulation of impinging jet arrays on a moving plate. *Int. J. Heat Mass Transf.* **2009**, *52*, 4894–4900. [CrossRef]
10. Chattopadhyay, H.; Saha, S.K. Turbulent flow and heat transfer from a slot jet impinging on a moving plate. *Int. J. Heat Fluid Flow* **2003**, *24*, 685–697. [CrossRef]
11. Chiriac, V.A.; Ortega, A. A numerical study of the unsteady flow and heat transfer in a transitional confined slot jet impinging on an isothermal surface. *Int. J. Heat Mass Transf.* **2002**, *45*, 1237–1248. [CrossRef]
12. Koseoglu, M.F.; Baskaya, S. The role of jet inlet geometry in impinging jet heat transfer, modeling and experiments. *Int. J. Therm. Sci.* **2010**, *49*, 1417–1426. [CrossRef]
13. Rehman, M.M.U.; Qu, Z.; Fu, R.; Xu, H. Numerical study on free-surface jet impingement cooling with nanoencapsulated phase-change material slurry and nanofluid. *Int. J. Heat Mass Transf.* **2017**, *109*, 312–325. [CrossRef]
14. Nakharintr, L.; Naphon, P. Magnetic field effect on the enhancement of nanofluids heat transfer of a confined jet impingement in mini-channel heat sink. *Int. J. Heat Mass Transf.* **2017**, *110*, 753–759. [CrossRef]
15. Selimefendigil, F.; Öztop, H.F. Pulsating nanofluids jet impingement cooling of a heated horizontal surface. *Int. J. Heat Mass Transf.* **2014**, *69*, 54–65. [CrossRef]
16. Ahmadi, M.H.; Ghazvini, M.; Sadeghzadeh, M.; Nazari, M.A.; Ghalandari, M. Utilization of hybrid nanofluids in solar energy applications: A review. *Nano-Struct. Nano-Objects* **2019**, *20*, 100386. [CrossRef]
17. Arshad, W.; Ali, H.M. Graphene nanoplatelets nanofluids thermal and hydrodynamic performance on integral fin heat sink. *Int. J. Heat Mass Transf.* **2017**, *107*, 995–1001. [CrossRef]
18. Hamzah, M.H.; Sidik, N.A.C.; Ken, T.L.; Mamat, R.; Najafi, G. Factors affecting the performance of hybrid nanofluids: A comprehensive review. *Int. J. Heat Mass Transf.* **2017**, *115*, 630–646. [CrossRef]
19. Kasaeian, A.; Daneshazarian, R.; Mahian, O.; Kolsi, L.; Chamkha, A.J.; Wongwises, S.; Pop, I. Nanofluid flow and heat transfer in porous media: A review of the latest developments. *Int. J. Heat Mass Transf.* **2017**, *107*, 778–791. [CrossRef]
20. Mohammed, K.A.; Talib, A.A.; Nuraini, A.; Ahmed, K. Review of forced convection nanofluids through corrugated facing step. *Renew. Sustain. Energy Rev.* **2017**, *75*, 234–241. [CrossRef]
21. Pordanjani, A.H.; Aghakhani, S.; Afrand, M.; Mahmoudi, B.; Mahian, O.; Wongwises, S. An updated review on application of nanofluids in heat exchangers for saving energy. *Energy Convers. Manag.* **2019**, *198*, 111886. [CrossRef]
22. Sahin, A.Z.; Uddin, M.A.; Yilbas, B.S.; Al-Sharafi, A. Performance enhancement of solar energy systems using nanofluids: An updated review. *Renew. Energy* **2020**, *145*, 1126–1148. [CrossRef]
23. Sajid, M.U.; Ali, H.M. Recent advances in application of nanofluids in heat transfer devices: A critical review. *Renew. Sustain. Energy Rev.* **2019**, *103*, 556–592. [CrossRef]
24. Qiu, L.; Zhu, N.; Feng, Y.; Michaelides, E.E.; Żyła, G.; Jing, D.; Zhang, X.; Norris, P.M.; Markides, C.N.; Mahian, O. A review of recent advances in thermophysical properties at the nanoscale: From solid state to colloids. *Phys. Rep.* **2020**, *843*, 1–81. [CrossRef]
25. Taherian, H.; Alvarado, J.L.; Languri, E.M. Enhanced thermophysical properties of multiwalled carbon nanotubes based nanofluids. Part 1: Critical review. *Renew. Sustain. Energy Rev.* **2018**, *82*, 4326–4336. [CrossRef]
26. Yang, L.; Jiang, W.; Ji, W.; Mahian, O.; Bazri, S.; Sadri, R.; Badruddin, I.A.; Wongwises, S. A review of heating/cooling processes using nanomaterials suspended in refrigerants and lubricants. *Int. J. Heat Mass Transf.* **2020**, *153*, 119611. [CrossRef]
27. Ambreen, T.; Kim, M.H. Influence of particle size on the effective thermal conductivity of nanofluids: A critical review. *Appl. Energy* **2020**, *264*, 114684. [CrossRef]
28. Bahiraei, M.; Heshmatian, S. Graphene family nanofluids: A critical review and future research directions. *Energy Convers. Manag.* **2019**, *196*, 1222–1256. [CrossRef]
29. Liang, G.; Mudawar, I. Review of single-phase and two-phase nanofluid heat transfer in macro-channels and micro-channels. *Int. J. Heat Mass Transf.* **2019**, *136*, 324–354. [CrossRef]
30. Li, Q.; Xuan, Y.; Yu, F. Experimental investigation of submerged single jet impingement using Cu-water nanofluid. *Appl. Therm. Eng.* **2012**, *36*, 426–433. [CrossRef]
31. Mahdavi, M.; Sharifpur, M.; Meyer, J.P.; Chen, L. Thermal analysis of a nanofluid free jet impingement on a rotating disk using volume of fluid in combination with discrete modelling. *Int. J. Therm. Sci.* **2020**, *158*, 106532. [CrossRef]
32. Jajja, S.A.; Ali, W.; Ali, H.M.; Ali, A.M. Water cooled minichannel heat sinks for microprocessor cooling: Effect of fin spacing. *Appl. Therm. Eng.* **2014**, *64*, 76–82. [CrossRef]

33. Manca, O.; Mesolella, P.; Nardini, S.; Ricci, D. Numerical study of a confined slot impinging jet with nanofluids. *Nanoscale Res. Lett.* **2011**, *6*, 188. [CrossRef] [PubMed]
34. Arshad, W.; Ali, H.M. Experimental investigation of heat transfer and pressure drop in a straight minichannel heat sink using TiO_2 nanofluid. *Int. J. Heat Mass Transf.* **2017**, *110*, 248–256. [CrossRef]
35. Selimefendigil, F.; Oztop, H.F. Jet impingement cooling and optimization study for a partly curved isothermal surface with CuO-water nanofluid. *Int. Commun. Heat Mass Transf.* **2017**, *89*, 211–218. [CrossRef]
36. Naphon, P.; Nakharintr, L.; Wiriyasart, S. Continuous nanofluids jet impingement heat transfer and flow in a micro-channel heat sink. *Int. J. Heat Mass Transf.* **2018**, *126*, 924–932. [CrossRef]
37. Mohammadpour, J.; Lee, A. Investigation of nanoparticle effects on jet impingement heat transfer: A review. *J. Mol. Liq.* **2020**, *316*, 113819. [CrossRef]
38. Kramer, L.R.; Mara, A.L.O.; Souza, S.S.; Ando, O.H. Analytical and numerical study for the determination of a thermoelectric generator's internal resistance. *Energies* **2019**, *12*, 3053. [CrossRef]
39. Kim, C.N. Development of a numerical method for the performance analysis of thermoelectric generators with thermal and electric contact resistance. *Appl. Therm. Eng.* **2018**, *1305*, 408–417. [CrossRef]
40. Zuckerman, N.; Lior, N. Jet impingement heat transfer: Physics, correlations, and numerical modeling. *Adv. Heat Transf.* **2006**, *39*, 565–631.
41. Sajjadi, H.; Delouei, A.A.; Izadi, M.; Mohebbi, R. Investigation of MHD natural convection in a porous media by double MRT lattice Boltzmann method utilizing MWCNT-Fe_3O_4/water hybrid nanofluid. *Int. J. Heat Mass Transf.* **2019**, *132*, 1087–1104. [CrossRef]
42. Brinkman, H. The viscosity of concentrated suspensions and solutions. *J. Chem. Phys.* **1952**, *20*, 571–581. [CrossRef]
43. Xue, Q. Model for thermal conductivity of carbon nanotube—Based composites. *Physica B* **2005**, *368*, 302–307. [CrossRef]
44. COMSOL A.B. *COMSOL Multiphysics v. 5.4*; COMSOL: Stockholm, Sweden, 2018.
45. Sharif, M.A. Heat transfer from an isothermally heated flat surface due to confined laminar twin oblique slot-jet impingement. *J. Therm. Sci. Eng. Appl.* **2015**, *7*. [CrossRef]
46. Sahoo, D.; Sharif, M. Numerical modeling of slot-jet impingement cooling of a constant heat flux surface confined by a parallel wall. *Int. J. Therm. Sci.* **2004**, *43*, 877–887. [CrossRef]
47. Chen, M.; Rosendahl, L.A.; Condra, T. A three-dimensional numerical model of thermoelectric generators in fluid power systems. *Int. J. Heat Mass Transf.* **2011**, *54*, 345–355. [CrossRef]